Flat-band ferromagnetism in the quasi-one-dimensional electride Y_2Cl_3 induced by hole doping

Shuyuan Liu,[1,*] Chongze Wang,[1] Bing Wang,[1,†] Yu Jia,[1,2,3] and J. Cho[1,4,‡]

[1]*Joint Center for Theoretical Physics, School of Physics and Electronics, Henan University, Kaifeng 475004, China*

[2]*Key Laboratory for Special Functional Materials of the Ministry of Education, Henan University, Kaifeng 475004, China*

[3]*Institute of Quantum Materials and Physics, Henan Academy of Sciences, Zhengzhou 450046, China*

[4]*Department of Physics and Research Institute for Natural Science, Hanyang University, 222 Wangsimni-ro, Seongdong-Ku, Seoul 04763, Republic of Korea*

(Received 28 March 2024; accepted 29 June 2024; published 10 July 2024)

Mielke and Tasaki's theoretical proposal of flatband ferromagnetism with the Hubbard model has attracted much attention due to the promising possibility of ferromagnetic order in electronic materials. Using first-principles density-functional theory calculations and tight-binding analysis, we present hole-doping-induced flatband ferromagnetism in the van der Waals layered insulating electride material Y_2Cl_3, whose structural framework consists of an array of weakly coupled one-dimensional (1D) Y wires. It is revealed that Y_2Cl_3, featuring a 1D paired, puckered diamond lattice of Y atoms, possesses three occupied valence states: the first- and second-highest (S_1 and S_2) states give rise to flatbands due to the destructive interference of Bloch wavefunctions, whereas the third-highest (S_3) state exhibits a dispersive band along the interstitial space within the paired diamond lattice. Upon partial hole doping of the S_1 band with a density larger than 0.3 holes per unit cell, we predict the emergence of ferromagnetism by satisfying the Stoner criterion, enabled by a high density of states at the Fermi level. Interestingly, the spin polarization of the S_1 band induces the nearly equal spin splitting of the S_2 and S_3 bands via the facilitated exchange interactions with the presence of interstitial anionic excess electrons. Our findings offer theoretical insights into an intricate flatband ferromagnetism in the experimentally synthesized 1D electride Y_2Cl_3 by hole doping, thereby enriching the family of 1D electride materials for spintronic applications.

DOI: 10.1103/PhysRevB.110.024413

I. INTRODUCTION

At the beginning of the 1990s, Mielke [1–3] and Tasaki [4] proposed an intriguing quantum state of flatband ferromagnetism based on the Hubbard model. Since then, many tight-binding (TB) Hubbard models have been investigated in a variety of lattices, i.e., Lieb [5], kagome [6], diamond [7], and checkboard [8], to demonstrate the emergence of flatband ferromagnetism. In such nontrivial lattices, flatbands are constructed by the destructive interference of Bloch wavefunctions [9–11]. The resultant localized electron wavefunctions in real space lead to the dominance of repulsive Coulomb interaction compared to the quenched kinetic energy. It has been theoretically predicted that, when the flatband is half-filled, arbitrary on-site Coulomb interaction $U > 0$ can induce a nontrivial ground state with ferromagnetic order [12]. More rigorous analyses of the flatband Hubbard models and their numerical simulations demonstrated that ferromagnetism remains undestroyed even in cases where the flatness and half-filling of a single band deviate from a perfectly half-filled flatband [13,14]. However, the challenge lies in finding real materials possessing the proper occupancy of a nearly flat band at the Fermi energy E_F, which exhibit a ferromagnetic ground state.

To date, a number of low-dimensional materials have been proposed as possible candidates for the emergence of flatband ferromagnetism. Based on spin-polarized density-functional theory (DFT) calculations, one-dimensional (1D) organic polymers [15], some 1D inorganic materials [16], two-dimensional (2D) metal-organic frameworks [17], and 2D carbon-based monolayers such as kagome graphene [18] and cyclic graphdiyne [19] were reported to have a nearly flatband crossing E_F, which leads to spin splitting via a Stoner instability with high density of states (DOS): i.e., the highly localized flatband electrons can align their spins to lower the potential energy of repulsive electron-electron interactions, according to the Pauli exclusion principle. Despite the longstanding theoretical efforts [20,21], the realization of crystalline flatband systems has been rarely accomplished in experiments. A recent discovery of flatbands in twisted bilayer graphene [22,23] has provided a platform to investigate many exotic quantum states including unconventional superconductivity [22], fractional quantum Hall states [24,25], and ferromagnetism [26]. Since the flatbands in twisted bilayer graphene are attributed to the localized electron wavefunctions in the moiré pattern at certain magic angles, their associated ferromagnetism was observed to survive only at low temperatures below a few degrees Kelvin, indicating a very weak magnetic coupling due to the large unit cell size. Compelling examples of crystalline flatband systems include various kagome metals such as Fe_3Sn_2 [27], FeSn [28], CoSn [29], and YMn_6Sn_6 [30], which have multivalence $3d$ electrons with a complicated

*Contact author: syliu814@gmail.com
†Contact author: wb@henu.edu.cn
‡Contact author: cho@henu.edu.cn

mixture of nearly flatbands and dispersive bands. It is thus difficult to study the intrinsic properties of isolated flatbands in these 3*d* transition-metal compounds. In this regard, the search for new materials having isolated flatbands is highly desired for exploration of flatband ferromagnetism.

Recently, as a special species of ionic crystal, low-dimensional inorganic electrides having interstitial anionic electrons separated from cationic atoms have been experimentally synthesized [31–34]. Since such anionic electrons are weakly bound to the constituent nuclei and are confined in interstitial spaces along 1D channels [35–37] or between 2D interlayers [38–42], electrides usually have the attractive features of high electrical conductivities and low work functions [31,43–45]. Specifically, the interplay between the novel electride properties and magnetism could be most promising for future applications in spintronics. Here, we identify the existence of isolated flatbands in the quasi-1D electride Y_2Cl_3 with the paired diamond lattice, which in turn hosts flatband ferromagnetism via hole doping. Notably, Y_2Cl_3 was synthesized experimentally several decades ago [46] and was recently identified as a 1D electride with anionic excess electrons [37]. However, the origin of the flatbands in Y_2Cl_3 has not been previously addressed.

In this article, using first-principles DFT calculations and TB analysis, we demonstrate that the quasi-1D electride Y_2Cl_3 with the paired, puckered diamond lattice of Y atoms has three occupied valence states where the first- and second-highest (S_1 and S_2) states exhibit a flatband feature due to the destructive interference of Bloch wavefunctions, whereas the third-highest (S_3) state represents a dispersive band. We find that the S_1, S_2, and S_3 states originate dominantly from the Y $d_{x^2-y^2}$, d_{yz}, and d_{xz} orbitals, respectively. However, the three states also have the anionic character of interstitial excess electrons residing inside the paired diamond lattice. By hole doping in the topmost S_1 band, the ferromagnetic order emerges via the Stoner instability with a high DOS at E_F. The resulting flatband ferromagnetism gives rise to the spin splitting of the S_1, S_2, and S_3 bands with nearly equal magnitudes, indicating that the exchange coupling between different Y-4*d* orbitals can be effectively facilitated with interstitial anionic electrons.

II. CALCULATIONAL METHODS

Our first-principles DFT calculations were performed using the Vienna *ab initio* simulation package with a plane-wave basis [47,48]. The interactions between core and valence electrons were described using the projector-augmented wave method [49], where the valence electron configurations of Y and Cl were considered as [$4s^2\ 4p^6\ 4d^1\ 5s^2$] and [$2s^2\ 3p^5$], respectively. The plane wave basis was employed with a kinetic energy cutoff of 550 eV, and the exchange-correlation energy was treated with the generalized-gradient approximation functional of Perdew *et al.* [50]. The *k*-point samplings were conducted using 8×8×6 *k* points for structure optimization and 16×16×12 *k* points for the DOS calculation. All atoms were allowed to relax along the calculated forces until all residual force components were less than 0.001 eV/Å. The effect of van der Waals (vdW) interactions between Y_2Cl_3 layers was taken into account by employing the optB86b functional [33,51]. In the hole-doping simulations, the hole density was tuned by removing electrons from the unit cell, with a jellium background with opposite charge added to maintain charge neutrality, and the atomic structures were optimized at different hole densities. The phonon calculations of Y_2Cl_3 were carried out using the QUANTUM ESPRESSO package [52], with 8×8×6 *k* points and 4×4×3 *q* points.

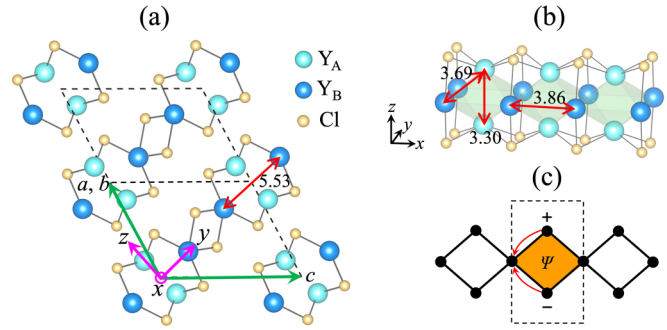

FIG. 1. (a) Optimized structure of bulk Y_2Cl_3. The crystal structure of Y_2Cl_3 has the space group C2/m with the lattice constants $a = 7.87$ Å, $b = 7.87$ Å, $c = 10.10$ Å, and the angles $\alpha = 28.4^\circ$ between a and b and $\beta = 116.8^\circ$ between b (or a) and c. Here, the dashed lines represent the primitive unit cell. The x-axis is taken along the Y wire. A single Y wire in the paired, puckered diamond lattice is illustrated in (b). The numbers in (a) and (b) represent the calculated Y − Y distances (in Å). Figure (c) presents a schematic diagram illustrating the destructive interference of Bloch wavefunctions in the 1D diamond lattice.

III. RESULTS AND DISCUSSION

We first optimize the atomic structure of Y_2Cl_3 using DFT calculations. Bulk Y_2Cl_3 was experimentally synthesized [46] and its structure is characterized by the 2D layered structure [see Fig. 1(a)], the basic building block of which is composed of the edge-sharing octahedral framework of six Y atoms. There are two kinds of Y atoms (designated as Y_A and Y_B) bridged by Cl atoms [37]. Such a 1D Y wire along the x-axis has the paired, puckered diamond lattice [see Fig. 1(b)], where the calculated Y − Y distances in the Y_6 octahedral are given in Figs. 1(a) and 1(b). Meanwhile, each Y wire is also bridged to neighboring wires by Cl atoms, forming an array of Y wires in the xy-plane. Note that a single 1D diamond lattice is one of the simplest quantum frustrated systems [53]. As depicted in Fig. 1(c), the destructive interference of Bloch wavefunctions in the 1D diamond lattice is expected to give rise to compact localized states and flatbands [53], which represent highly degenerate manifold states of electrons, as discussed below.

Figure 2(a) shows the calculated band structure of bulk Y_2Cl_3, together with the partial density of states (PDOS) for the Y 4*d* and Cl 3*p* orbitals. There are three valence states S_1, S_2, and S_3 with a band gap of 1.01 eV at the Γ point, in good agreement with a previous [37] DFT calculation. The S_1 (S_2) state is represented by a rather flat band with a narrow bandwidth of 0.17 (0.34) eV, whereas the S_3 state exhibits a dispersive band with a bandwidth of 0.74 eV. As shown in Fig. 2(a) and Supplemental Fig. S1 [54], the PDOS and band projection onto different orbitals indicate that the S_1, S_2,

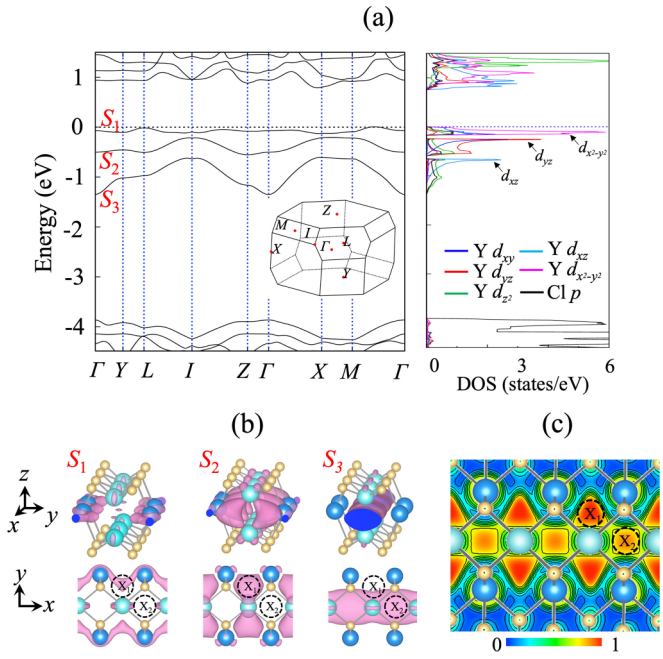

FIG. 2. (a) Calculated band structure of bulk Y_2Cl_3, together with the PDOS for the Y $4d$ and Cl $3p$ orbitals. The inset of (a) shows the brillouin zone of the primitive unit cell. In (b), the perspective and top views of the charge characters of the S_1, S_2, and S_3 states are displayed with an isosurface of 0.04 $e/Å^3$. In (c), the calculated ELF is drawn on the $(20\bar{1})$ plane with a contour spacing of 0.1. The dashed circles in (b) and (c) represent the Wigner − Seitz spheres of the X_1 and X_2 anions, the centers of which are (-1.928, 1.690, 0) and (0, 0, 0) in Cartesian coordinates, respectively.

and S_3 states originate dominantly from $d_{x^2-y^2}$, d_{yz}, and d_{xz} orbitals, respectively. Meanwhile, the fully occupied Cl $3p$ orbitals are located around −4.0 eV below E_F, indicating an anionic character of Cl^- with cationic Y atoms. It is worth noting that the S_1, S_2, and S_3 states also have a characteristic feature of anionic excess electrons residing in interstitial spaces inside the paired diamond lattice, as discussed below.

In Fig. 2(b), the charge characters of the S_1, S_2, and S_3 states are displayed by integrating the charge densities of Bloch wavefunctions over the Brillouin zone. We find that the S_1 state with the $d_{x^2-y^2}$ orbital character of Y_B exhibits an electron distribution mostly confined inside the paired diamond lattice with a minimal spread around the Y_A atoms. Such an electron localization may be related to a flatband-induced localization due to a destructive interference in the paired diamond lattice, as discussed below. Similarly, the S_2 state with the d_{yz} orbital character of Y_A exhibits a localized electron distribution inside the paired diamond lattice with a minimal spread around the Y_B atoms [see Fig. 2(b)]. Meanwhile, as shown in Fig. 2(b), the S_3 state with the d_{xz} orbital character of Y_A exhibits a strong delocalized electron distribution along the x-axis inside the paired diamond lattice. To identify the electride characteristics of Y_2Cl_3, the electron localization function (ELF) is plotted in Fig. 2(c). We find the presence of anionic excess electrons at the positions marked as X_1 and X_2 in the interstitial space inside the paired diamond lattice. These local maxima positions of ELF in the xy-plane agree well with those of a previous DFT calculation [37]. We

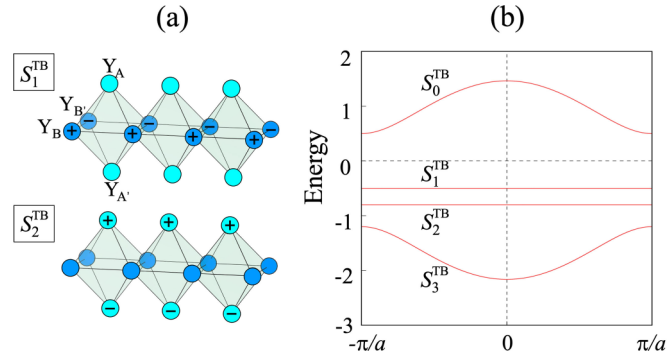

FIG. 3. (a) Calculated eigenvector signs of the S_1^{TB} and S_2^{TB} flatbands and (b) band structure in the TB analysis, with the parameters $t = -0.4$, $t_A = -0.2$, $t_B = 0.5$, and $\Delta = -1.0$. These parameters were selected to match the TB eigenvalues with those obtained from the DFT calculation of bulk Y_2Cl_3 at $k = \pi/a$. In (a), the four Y atoms in the unit cell are designated as Y_A, $Y_{A'}$, Y_B, and $Y_{B'}$.

further examine how largely these interstitial anionic electrons contribute to the S_1, S_2, and S_3 states by calculating the PDOS for X_1 and X_2 anions with a Wigner-Seitz radius of 1.0 Å [see the dashed circles in Fig. 2(c)]. As shown in Supplemental Fig. S2, all S_1, S_2, and S_3 states have much contribution from X_1 and X_2 anions, indicating a strong hybridization between Y-$4d$ cationic and interstitial anionic electrons. Specifically, the S_2 (S_3) state has a more significant contribution from the X_1 (X_2) anion, which may result in a larger bandwidth compared to the S_1 band [see Fig. 2(a)].

To gain insight into the nature of the S_1, S_2, and S_3 states in Y_2Cl_3, we conduct a TB analysis for the single paired diamond lattice, comprising four Y atoms per unit cell, designated Y_A, $Y_{A'}$, Y_B, and $Y_{B'}$ in Fig. 3(a). Considering the Y oxidation state of 2+ in Y_2Cl_3 [55,56], we focus solely on a single orbital TB analysis for this diamond lattice.

$$H = \begin{pmatrix} \Delta & t_A & h & h \\ t_A & \Delta & h & h \\ h^* & h^* & 0 & t_B \\ h^* & h^* & t_B & 0 \end{pmatrix}, \tag{1}$$

where Δ represents the on-site energy difference between Y_A ($Y_{A'}$) and Y_B ($Y_{B'}$) sites; t_A, t_B, and t represent the nearest-neighbor hopping parameters of $Y_A \leftrightarrow Y_{A'}$, $Y_B \leftrightarrow Y_{B'}$, and Y_A ($Y_{A'}$) $\leftrightarrow$ Y_B ($Y_{B'}$), respectively; and $h = t + te^{-ika}$ (a: the lattice constant along the x-axis). By solving the TB Hamiltonian, we obtain two flatbands S_1^{TB} and S_2^{TB} with the eigenvalues of $E_1 = -t_B$ and $E_2 = -t_A + \Delta$, and two dispersive bands S_0^{TB} and S_3^{TB} [see Fig. 3(b)]. The eigenvector of the S_1^{TB} flatband is $\{0, 0, 1, -1\}$, indicating the presence of nodes at Y_A and $Y_{A'}$, as depicted in Fig. 3(a). Meanwhile, the eigenvector of the S_2^{TB} flatband is $\{1, -1, 0, 0\}$ with the nodes at Y_B and $Y_{B'}$. These localized eigenstates are attributed to the destructive interference of wavefunctions in the paired diamond lattice. By comparing the DFT [Fig. 2(a)] and TB [Fig. 3(b)] band structures, we can determine that the S_1 and S_3 bands originate from flatbands S_1^{TB} and S_2^{TB}, respectively. Note that the S_1^{TB} band is unoccupied because of four valence electrons in the TB model. However, for Y_2Cl_3, the S_1 band is fully occupied by including two anionic excess electrons

TABLE I. Calculated bond angles (°) and bond lengths (Å) in the Y_6 octahedra without and with hole doping.

n_h (e)	$\angle Y_A$-Cl-Y_B	$\angle Y_A$-Y_B-Y_A	$\angle Y_B$-Y_A-Y_B	d_{Y_A-Cl}	d_{Y_B-Cl}	$d_{Y_A-Y_B}$
0	84.25	52.73	93.85	2.77	2.72	3.69
0.3	84.81	52.83	94.55	2.76	2.71	3.68
0.5	84.95	52.91	94.66	2.74	2.70	3.67

per unit cell [see Fig. 2(a)]. In contrast to the perfect flatness of the S_1^{TB} and S_2^{TB} bands in the TB model, the flatness of the S_1 and S_2 bands in Y_2Cl_3 is weakened due to the presence of interstitial anionic electrons and intralayer/interlayer interactions.

By hole doping in nonmagnetic, insulating 2D monolayers such as GaSe [57] and In_2Se_3 [58], a Stoner-type magnetic instability was predicted to drive itinerant ferromagnetism: i.e., the hole doping in the narrow valence bands induces spin polarization via exchange interaction, where spin-polarized electrons remain farther apart by Fermi statistics to lower the Coulomb repulsion energy. Similarly, we introduce holes into the narrow S_1 band in Y_2Cl_3 to examine the possibility of ferromagnetic instability. Table I presents the calculated bond angles and bond lengths in the Y_6 octahedra without and with hole doping. We find that at a hole density of $n_h = 0.3e$ ($0.5e$), the angles $\angle Y_A$-Cl-Y_B, $\angle Y_A$-Y_B-Y_A, and $\angle Y_B$-Y_A-Y_B are 84.81° (84.95°), 52.83° (52.91°), and 94.55° (94.66°), respectively, showing a slight increase compared to the angles without hole doping (84.25°, 52.73°, and 93.85°). Meanwhile, the bond lengths d_{Y_A-Cl}, d_{Y_B-Cl}, and $d_{Y_A-Y_B}$ are 2.76 (2.74), 2.71 (2.70), and 3.68 (3.67) Å at $n_h = 0.3e$ ($0.5e$), respectively, showing a slight decrease compared to the bond lengths without hole doping (2.77, 2.72, and 3.69 Å). Additionally, we compare the charge character of the S_1 state at $n_h = 0$, 0.3, and $0.5e$ in Supplemental Fig. S3. Here, each charge character is displayed by integrating the charge densities of the occupied S_1 state over the Brillouin zone. We find that the electron distribution of the S_1 state having the $d_{x^2-y^2}$ orbital character of Y_B slightly decreases with hole doping. As depicted in Supplemental Fig. S4, the bandwidths of S_1, S_2, and S_3 without hole doping are estimated to be 0.17, 0.34, and 0.74 eV, respectively. With a hole density of $n_h = 0.3e$ ($0.5e$), the bandwidths of S_1, S_2, and S_3 change slightly to 0.20 (0.21), 0.32 (0.29), and 0.73 (0.71) eV, respectively [59]. As shown in Fig. 4(a), the ferromagnetic state emerges as the hole density n_h increases. For $n_h > 0.3e$ per unit cell (equivalent to 8.5×10^{13} cm^{-2}), the ferromagnetic state becomes more thermodynamically stable than the nonmagnetic state with an energy gain of spin-polarization energy E_{spin} [see Fig. 4(a)]. Note that the typical doping densities are in a range between 5×10^{12} cm^{-2} and 8×10^{14} cm^{-2} [60]. Based on phonon calculations, we confirm that the ferromagnetic structure is dynamically stable without imaginary phonon frequencies (see Supplemental Fig. S5 [54]). The calculated magnetic moment M increases monotonically as n_h increases [see Fig. 4(a)]. We find that M jumps sharply to 0.4 μ_B at $n_h = 0.4e$ and reaches 1 μ_B at $n_h = 1.0e$. Due to an increased DOS at E_F under hole doping, the Stoner criterion can be fulfilled to drive a ferromagnetic instability. Indeed, we find that for $n_h = 0.5e$, the nonmagnetic state has a high DOS of 5.18 states/eV per spin at E_F [see Fig. 4(b)]. Consequently, the Stoner criterion $I \cdot D(E_F)$ is larger than 1, where the Stoner parameter $I = 1.36$ eV is estimated from the exchange splitting of 0.17 eV [see Fig. 4(c) and Supplemental Fig. S6] divided by $M = 0.125$ μ_B per Y atom. It is thus demonstrated that the partially hole-doped S_1 band at the top of the valence states induces a ferromagnetic instability via a Stoner mechanism with the exchange splitting of other electronic states, as discussed below.

Figures 4(c) and 4(d) show the ferromagnetic band structures of Y_2Cl_3 at $n_h = 0.5e$ and $1.0e$, respectively. We find the strong spin splitting of the S_1, S_2, and S_3 bands. For $0.3e < n_h < 1.0e$, the Fermi level crosses only the spin-down S_1 band, yielding a half-metal state with fully polarized spin transport. Meanwhile, at $n_h = 1.0e$, the system becomes a ferromagnetic semiconductor with a narrow gap of ~70 meV [see Fig. 4(d)]. Interestingly, for $n_h = 0.5e$ ($1.0e$), the spin splitting energies of the S_1, S_2, and S_3 bands are the nearly same as 0.15 (0.30), 0.12 (0.30), and 0.11 (0.33) eV at the Γ point, respectively [see Figs. 4(c) and 4(d)]. This result indicates that the ferromagnetic instability of the S_1 band

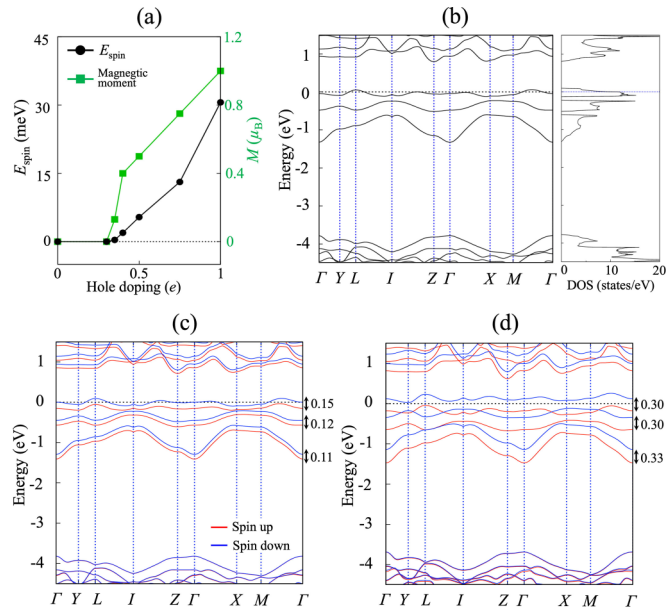

FIG. 4. (a) Calculated spin-polarization energy E_{spin} and magnetic moment M of bulk Y_2Cl_3 as a function of n_h. The units of E_{spin} and M are per unit cell. The calculated band structure and DOS of the nonmagnetic state at $n_h = 0.5e$ are displayed in (b). The band structures of the ferromagnetic state at $n_h = 0.5e$ and $1.0e$ are displayed in (c) and (d), respectively. The numbers in (c) and (d) represent the spin splitting energies (in eV) of the S_1, S_2, and S_3 bands at the Γ point.

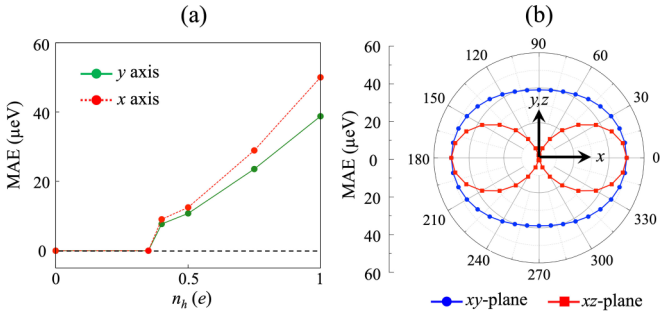

FIG. 5. (a) Calculated MAE of hole-doped ferromagnetic Y_2Cl_3 as a function of n_h. The angular dependence of MAE at $n_h = 1.0e$ is displayed on the xy- and xz-planes. Here, the MAE is defined as the energy difference relative to the total energy for the out-of-plane magnetization axis.

simultaneously induces the spin splitting of the S_2 and S_3 bands. The similar magnitudes of exchange splitting in the S_1, S_2, and S_3 states imply that these three states are cooperative for stabilizing the long-range ferromagnetic order. It is worth noting that the S_1, S_2, and S_3 states exhibit significant contributions from X_1 and X_2 anions, indicating strong hybridization between Y-4d cationic and interstitial anionic electrons (see Supplemental Fig. S2). To assess the impact of anionic excess electrons on the Stoner criterion, we calculated the PDOS arising from Y-4d and anionic electrons for the nonmagnetic configuration at $n_h = 0.5e$. Our analysis reveals that the PDOS of X_1 and X_2 anionic electrons is about 30% of that of Y-4d electrons (see Supplemental Fig. S7), suggesting a notable contribution of anionic excess electrons to ferromagnetic instability. It is well established that in ferromagnetic electrides, the exchange interactions between localized cationic spins can be effectively mediated by interstitial anionic electrons [32,40]. Considering the hybridization between Y-4d cationic and interstitial anionic electrons in the S_1, S_2, and S_3 states [see Fig. 2(a) and Supplemental Fig. S2], we can say that the exchange coupling between different Y-4d orbitals can be effectively facilitated with interstitial anionic electrons.

It is worth noting that 2D magnetic systems described by the isotropic Heisenberg model cannot attain a long-range magnetic order at any finite temperature due to thermal spin fluctuations imposed by the Mermin-Wagner theorem [61]. However, such thermal agitation can be suppressed by magnetocrystalline anisotropy, leading to the stabilization of 2D magnetism [62]. In Fig. 5(a), the calculated magnetic anisotropy energy (MAE) of hole-doped ferromagnetic Y_2Cl_3 is displayed as a function of n_h. We find that the MAE along the x (y) direction increases with increasing n_h, such as 12.5 (10.8), 28.9 (23.6), and 50.0 (38.8) μeV at $n_h = 0.5$, 0.75, and 1.0e, respectively. Here, the positive MAE values indicate that the easy magnetization axis points along the z direction: i.e., the spins prefer to align along the out-of-plane direction. Figure 5(b) shows the angular dependence of the MAE on the xy- and xz-planes at $n_h = 1.0e$, revealing significantly more anisotropic behavior on the xz-plane compared to the xy-plane. Therefore, hole-doped ferromagnetic Y_2Cl_3 exhibits triaxial magnetic anisotropy, with the easy magnetization axis along the z direction, the intermediate magnetization axis along the y direction, and the hard magnetization axis along the x direction.

So far, the control of long-range magnetic orders via doped free carriers has been extensively studied both theoretically and experimentally. Jiang *et al*. [63] and Zheng *et al*. [64] have demonstrated the capability of doped free carriers to manipulate magnetic orders. Moreover, the efficient manipulation of free carriers by electric gating in 2D materials has been well established [65]. Therefore, it is anticipated that the hole-doped flatband ferromagnetism in the 2D vdW layered electride Y_2Cl_3 can be realized through gate biasing in magnetic tunnel junctions. Recent advancements have shown that high doping carrier densities on the order of $\sim 10^{14}$ cm^{-2} can be achieved in 2D materials via electrolyte gating [66–68], which is close to the present hole-doping range of $n_h > 0.3e$. Additionally, nonmagnetic acceptor impurities can induce hole doping in 2D materials, leading to a shift of the Fermi level toward the valence bands and facilitating the transition from a nonmagnetic to a ferromagnetic state.

IV. CONCLUSIONS

Our first-principles DFT calculations and TB analysis have proposed the emergence of flatband ferromagnetism in the layered insulating electride material Y_2Cl_3 via hole doping. Specifically, we revealed that Y_2Cl_3 exhibits flatbands due to the destructive interference of Bloch wavefunctions in a 1D paired, puckered diamond lattice. Furthermore, upon partial hole doping of the topmost valence band with a density larger than 0.3 holes per unit cell, we predicted the ferromagnetic instability by satisfying the Stoner criterion, enabled by a high DOS at the Fermi level. The present work provides a novel platform to investigate the intriguing interplay between electride materials and flatband ferromagnetism, holding promise for future spintronics technologies.

ACKNOWLEDGMENTS

This work was supported by the National Natural Science Foundation of China (Grant No. 12104130). Y.J. acknowledges National Natural Science Foundation of China (Grant No. 12074099) and J.C. acknowledges the National Research Foundation of Korea grant funded by the Korean Government (Grant No. RS202300218998).

S.L. and C.W. contributed equally to this work.

[1] A. Mielke, Ferromagnetic ground states for the Hubbard model on line graphs, J. Phys. A: Math. Gen. **24**, L73 (1991).

[2] A. Mielke, Ferromagnetism in the Hubbard model on line graphs and further considerations, J. Phys. A: Math. Gen. **24**, 3311 (1991).

[3] A. Mielke, Exact ground states for the Hubbard model on the Kagome lattice, J. Phys. A: Math. Gen. **25**, 4335 (1992).

[4] H. Tasaki, Ferromagnetism in the Hubbard models with degenerate single-electron ground states, Phys. Rev. Lett. **69**, 1608 (1992).

[5] A. Julku, S. Peotta, T. I. Vanhala, D.-H. Kim, and P. Törmä, Geometric origin of superfluidity in the Lieb-lattice flat band, Phys. Rev. Lett. **117**, 045303 (2016).

[6] X. Wu, T. Schwemmer, T. Müller, A. Consiglio, G. Sangiovanni, D. D. Sante, Y. Iqbal, W. Hanke, A. P. Schnyder, M. M. Denner, M. H. Fischer, T. Neupert, and R. Thomale, Nature of unconventional pairing in the kagome superconductors AV_3Sb_5 (A=K, Rb, Cs), Phys. Rev. Lett. **127**, 177001 (2021).

[7] L. Morales-Inostroza and R. A. Vicencio, Simple method to construct flat-band lattices, Phys. Rev. A **94**, 043831 (2016).

[8] K. Sun, Z. Gu, H. Katsura, and S. Das Sarma, Nearly flatbands with nontrivial topology, Phys. Rev. Lett. **106**, 236803 (2011).

[9] Y.-F. Wang, Z.-C. Gu, C.-D. Gong, and D. N. Sheng, Fractional quantum Hall effect of hard-core bosons in topological flat bands, Phys. Rev. Lett. **107**, 146803 (2011).

[10] Z. Liu, Z.-F. Wang, J.-W. Mei, Y.-S. Wu, and F. Liu, Flat Chern band in a two-dimensional organometallic framework, Phys. Rev. Lett. **110**, 106804 (2013).

[11] Z. Liu, F. Liu, and Y.-S. Wu, Exotic electronic states in the world of flat bands: From theory to material, Chin. Phys. B **23**, 077308 (2014).

[12] H. Tasaki, From Nagaoka's ferromagnetism to flat-band ferromagnetism and beyond, Prog. Theor. Phys. **99**, 489 (1998).

[13] R. Arita, Y. Shimoi, K. Kuroki, and H. Aoki, Flat-band ferromagnetism induced by off-site repulsions, Phys. Rev. B **57**, 10609 (1998).

[14] H. Tasaki, Hubbard model and the origin of ferromagnetism, Eur. Phys. J. B **64**, 365 (2008).

[15] R. Arita, Y. Suwa, K. Kuroki, and H. Aoki, Gate-induced band ferromagnetism in an organic polymer, Phys. Rev. Lett. **88**, 127202 (2002).

[16] S. Guo, H. E. M. Warden, and R. J. Cava, Structural diversity in oxoiridates with 1D IrnO3(n+1) chain fragments and flat Bands, Inorg. Chem. **61**, 10043 (2022).

[17] M. G. Yamada, T. Soejima, N. Tsuji, D. Hirai, M. Dinca, and H. Aoki, First-principles design of a half-filled flat band of the kagome lattice in two-dimensional metal-organic frameworks, Phys. Rev. B **94**, 081102(R) (2016).

[18] Y. Chen, S. Xu, Y. Xie, C. Zhong, C. Wu, and S. B. Zhang, Ferromagnetism and Wigner crystallization in kagome graphene and related structures, Phys. Rev. B **98**, 035135 (2018).

[19] J.-W. Rhim, K. Kim, and B.-J. Yang, Quantum distance and anomalous Landau levels of flat bands, Nature (London) **584**, 59 (2020).

[20] D. Călugăru, A. Chew, L. Elcoro, N. Regnault, Z.-D. Song, and B. A. Bernevig, General construction and topological classification of all magnetic and non-magnetic flat bands, Nat. Phys. **18**, 185 (2022).

[21] N. Regnault, Y. Xu, M.-R. Li, D.-S. Ma, M. Jovanovic, A. Yazdani, S. S. P. Parkin, C. Felser, L. M. Schoop, N. P. Ong, R. J. Cava, L. Elcoro, Z.-D. Song, and B. A. Bernevig, Catalogue of flat-band stoichiometric materials, Nature (London) **603**, 824 (2022).

[22] Y. Cao, V. Fatemi, S. Fang, K. Watanabe, T. Taniguchi, E. Kaxiras, and P. Jarillo-Herrero, Unconventional superconductivity in magic-angle graphene superlattices, Nature (London) **556**, 43 (2018).

[23] S. Lisi *et al.*, Observation of flat bands in twisted bilayer graphene, Nat. Phys. **17**, 189 (2021).

[24] E. Tang, J.-W. Mei, and X.-G. Wen, High-temperature fractional quantum Hall states, Phys. Rev. Lett. **106**, 236802 (2011).

[25] T. Neupert, L. Santos, C. Chamon, and C. Mudry, Fractional quantum Hall states at zero magnetic field, Phys. Rev. Lett. **106**, 236804 (2011).

[26] A. L. Sharpe, E. J. Fox, A. W. Barnard, J. Finney, K. Watanabe, T. Taniguchi, M. A. Kastner, and D. Goldhaber-Gordon, Emergent ferromagnetism near three-quarters filling in twisted bilayer graphene, Science **365**, 605 (2019).

[27] Z. Lin, J. H. Choi, Q. Zhang, W. Qin, S. Yi, P. Wang. L. Li, Y. Wang, H. Zhang, Z. Sun, L. Wei, S. Zhang, T. Guo, Q. Lu, J.-H. Cho, C. Zeng, and Z. Zhang, Flatbands and emergent ferromagnetic ordering in Fe_3Sn_2 kagome lattices, Phys. Rev. Lett. **121**, 096401 (2018).

[28] Z. Lin, C. Wang, P. Wang, S. Yi, L. Li, Q. Zhang, Y. Wang, Z. Wang, H. Huang, Y. Sun, Y. Huang, D. Shen, D. Feng, Z. Sun, J.-H. Cho, C. Zeng, and Z. Zhang, Dirac fermions in antiferromagnetic FeSn kagome lattices with combined space inversion and time-reversal symmetry, Phys. Rev. B **102**, 155103 (2020).

[29] M. Kang, S. Fang, L. Ye, H. C. Po, J. Denlinger, C. Jozwiak, A. Bostwick, E. Rotenberg, E. Kaxiras, J. G. Checkelsky, and R. Comin, Topological flat bands in frustrated kagome lattice CoSn, Nat. Commun. **11**, 4004 (2020).

[30] M. Li, Q. Wang, G. Wang, Z. Yuan, W. Song, R. Lou, Z. Liu, Y. Huang, Z. Liu, H. Lei, Z. Yin, and S. Wang, Dirac cone, flat band and saddle point in kagome magnet YMn_6Sn_6, Nat. Commun. **12**, 3129 (2021).

[31] K. Lee, S. W. Kim, Y. Toda, S. Matsuishi, and H. Hosono, Dicalcium nitride as a two-dimensional electride with an anionic electron layer, Nature (London) **494**, 336 (2013).

[32] S. Y. Lee, J.-Y. Hwang, J. Park, C. N. Nandadasa, Y. Kim, J. Bang, K. Lee, K. H. Lee, Y. Zhang, Y. Ma, H. Hosono, Y. H. Lee, S.-G. Kim, and S. W. Kim, Ferromagnetic quasi-atomic electrons in two-dimensional electride, Nat. Commun. **11**, 1526 (2020).

[33] H. Y. Song, B. I. Yoo, J.-H. Choi, S.-H. Kang, J. Bang, W. Li, C. N. Nandadasa, D. Thapa, D. Yoon, M. J. Han, K. H. Lee, S. G. Kim, K. Lee, and S. W. Kim, Van der Waals electride: Toward intrinsic two-dimensional ferromagnetism of spin-polarized anionic electrons, Mater. Today Phys. **20**, 100473 (2021).

[34] S. H. Kang, J. Bang, K. Chung, C. N. Nandadasa, G. Han, S. Lee, K. H. Lee, K. Lee, Y. Ma, S. H. Oh, S.-G. Kim, Y.-M. Kim, and S. W. Kim, Water- and acid-stable self-passivated dihafnium sulfide electride and its persistent electrocatalytic reaction, Sci. Adv. **6**, eaba7416 (2020).

[35] Y. Lu, J. Li, T. Tada, Y. Toda, S. Ueda, T. Yokoyama, M. Kitano, and H. Hosono, Water durable electride Y_5Si_3: Electronic structure and catalytic activity for ammonia synthesis, J. Am. Chem. Soc. **138**, 3970 (2016).

[36] Y. Zhang, Z. Xiao, T. Kamiya, and H. Hosono, Electron confinement in channel spaces for one-dimensional electride, J. Phys. Chem. Lett. **6**, 4966 (2015).

[37] B. Wan, Y. Lu, Z. Xiao, Y. Muraba, J. Kim, D. Huang, L. Wu, H. Gou, J. Zhang, and F. Gao, Identifying quasi-2D and 1D electrides in yttrium and scandium chlorides via geometrical identification, npj Comput. Mater. **4**, 77 (2018).

[38] J. Park, K. Lee, S. Y. Lee, C. N. Nandadasa, S. Kim, K. H. Lee, Y. H. Lee, H. Hosono, S.-G. Kim, and S. W. Kim, Strong localization of anionic electrons at interlayer for electrical and

magnetic anisotropy in two-dimensional Y_2C electride, J. Am. Chem. Soc. **139**, 615 (2017).

[39] T. Inoshita, S. Jeong, N. Hamada, and H. Hosono, Exploration for two-dimensional electrides via database screening and *ab initio* calculation, Phys. Rev. X **4**, 031023 (2014).

[40] S. Liu, C. Wang, L. Liu, J.-H. Choi, H.-J. Kim, Y. Jia, C. H. Park, and J.-H. Cho, Ferromagnetic Weyl fermions in two-dimensional layered electride Gd_2C, Phys. Rev. Lett. **125**, 187203 (2020).

[41] S. Liu, C. Wang, H. Jeon, J. Kim, and J.-H. Cho, Interlayer exchange interaction driven topological phase transition in antiferromagnetic electride Gd_2O, Phys. Rev. B **105**, L041406 (2022).

[42] S. Liu, C. Wang, H. Jeon, Y. Jia, and J.-H. Cho, Emerging two-dimensional magnetism in nonmagnetic electrides Hf_2X (X=S, Se, Te), Phys. Rev. B **105**, L220401 (2022).

[43] M. Kitano, Y. Inoue, Y. Yamazaki, F. Hayashi, S. Kanbara, S. Matsuishi, T. Yokoyama, S.-W. Kim, M. Hara, and H. Hosono, Ammonia synthesis using a stable electride as an electron donor and reversible hydrogen store, Nat. Chem. **4**, 934 (2012).

[44] Y. Liu, H. Wei, X. Wang, H. Jiao, and X. Jing, Preparation and electrical properties of inorganic electride $Y_2Ti_2O_6$2+(2e-), RSC Adv. **12**, 28414 (2022).

[45] S. Liu, W. Li, S. W. Kim, and J.-H. Choi, Decisive role of interlayer ionic couplings for the electronic properties of two-dimensional layered electrides, J. Phys. Chem. C **124**, 1398 (2020).

[46] H. Mattausch, J. B. Hendricks, R. Eger, J. D. Corbett, and A. Simon, Reduced halides of yttrium with strong metal-metal bonding: Yttrium monochloride, monobromide, sesquichloride, and sesquibromide, Inorg. Chem. **19**, 2128 (1980).

[47] G. Kresse and J. Hafner, *Ab initio* molecular dynamics for open-shell transition metals, Phys. Rev. B **48**, 13115 (1993).

[48] G. Kresse and J. Furthmüller, Efficiency of *ab-initio* total energy calculations for metals and semiconductors using a plane-wave basis set, Comput. Mater. Sci. **6**, 15 (1996).

[49] P. E. Blöchl, Projector augmented-wave method, Phys. Rev. B **50**, 17953 (1994).

[50] J. P. Perdew, K. Burke, and M. Ernzerhof, Generalized gradient approximation made simple, Phys. Rev. Lett. **77**, 3865 (1996); **78**, 1396(E) (1997).

[51] J. Klimeš, D. R. Bowler, and A. Michaelides, Chemical accuracy for the van der Waals density functional, J. Phys.: Condens. Matter **22**, 022201 (2010).

[52] P. Giannozzi *et al.*, QUANTUM ESPRESSO: A modular and open-source software project for quantum simulations of materials, J. Phys.: Condens. Matter **21**, 395502 (2009).

[53] D. Leykam, A. Andreanov, and S. Flach, Artificial flat band systems: From lattice models to experiments, Adv. Phys. **3**, 1473052 (2018).

[54] See Supplemental Material at http://link.aps.org/supplemental/10.1103/PhysRevB.110.024413 for the band structures of bulk Y_2Cl_3 projected onto Y_A and Y_B*d* orbitals, the projected DOS for X_1 and X_2 anions, the partial charge density of the occupied S_1 state with hole doping, the bandwidths of Y_2Cl_3 without and with hole doping, the phonon spectra of hole-doped Y_2Cl_3, the Stoner instability of hole-doped Y_2Cl_3, and the calculated PDOS arising from Y-4*d* and anionic electrons.

[55] N. B. Mikheev, L. N. Auerman, I. A. Rumer, A. N. Kamenskaya, and M. Z. Kazakevich, The anomalous stabilisation of the oxidation state 2+ of lanthanides and actinides, Russ. Chem. Rev. **61**, 990 (1992).

[56] G. Meyer and H. J. Meyer, Unusual valences in rare-earth halides, Chem. Mater. **4**, 1157 (1992).

[57] T. Cao, Z. Li, and S. G. Louie, Tunable magnetism and half-metallicity in hole-doped monolayer GaSe, Phys. Rev. Lett. **114**, 236602 (2015).

[58] C. Liu, B. Wang, G. Jia, P. Liu, H. Yin, S. Guan, and Z. Cheng, Tunable magnetism in ferroelectric α-In_2Se_3 by hole-doping, Appl. Phys. Lett. **118**, 072902 (2021).

[59] Unlike conventional 2D electride materials, which typically feature anionic excess electrons residing between interlayers, the quasi-1D electride Y_2Cl_3 harbors anionic excess electrons within the paired diamond lattice. Consequently, the interlayer coupling in the 2D vdW layered Y_2Cl_3 electride is expected to be much weaker than in conventional 2D electrides. As shown in Fig. S3, the electron distribution of the S_1 state, characterized by the $d_{x^2-y^2}$ orbital of Y_B, decreases slightly with hole doping. Similarly, the bandwidths of the S_1, S_2, and S_3 states exhibit minimal variations with hole doping (see Fig. S4), indicating that electronic localization is only slightly affected by hole doping.

[60] R. Meng, L. D. C. Pereira, J.-P. Locquet, V. Afanasev, G. Pourtois, and M. Houssa, Hole-doping induced ferromagnetism in 2D materials, npj Comput. Mater. **8**, 230 (2022).

[61] N. D. Mermin and H. Wagner, Absence of ferromagnetism or antiferromagnetism in one- or two-dimensional isotropic Heisenberg models, Phys. Rev. Lett. **17**, 1133 (1966).

[62] S. Hope, B.-Ch. Choi, P. J. Bode, and J. A. C. Bland, Direct observation of the stabilization of ferromagnetic order by magnetic anisotropy, Phys. Rev. B **61**, 5876 (2000).

[63] S. Jiang, L. Li, Z. Wang, K. F. Mak, and J. Shan, Controlling magnetism in 2D CrI_3 by electrostatic doping, Nat. Nanotechnol. **13**, 549 (2018).

[64] G. Zheng, W.-Q. Xie, S. Albarakati, M. Algarni, C. Tan. Y. Wang, J. Peng, J. Partridge, L. Farrar, J. Yi, Y. Xiong, M. Tian, Y.-J. Zhao, and L. Wang, Gate-tuned interlayer coupling in van der Waals ferromagnet Fe_3GeTe_2 nanoflakes, Phys. Rev. Lett. **125**, 047202 (2020).

[65] K. S. Novoselov, A. Mishchenko, A. Carvalho, and A. H. Castro Neto, 2D materials and van der Waals heterostructures, Science **353**, aac9439 (2016).

[66] Y. Zhang, T. Oka, R. Suzuki, J. Ye, and Y. Iwasa, Electrically switchable chiral light-emitting transistor, Science **344**, 725 (2014).

[67] J. T. Ye, S. Inoue, K. Kobayashi, Y. Kasahara, H. T. Yuan, H. Shimotani, and Y. Iwasa, Liquid-gated interface superconductivity on an atomically flat film, Nat. Mater. **9**, 125 (2010).

[68] D. K. Efetov and P. Kim, Controlling electron-phonon interactions in graphene at ultrahigh carrier densities, Phys. Rev. Lett. **105**, 256805 (2010).